Reduction of Fast Spin Echo Cusp Artifact Using a Slice-Tilting Gradient

Novena Rangwala[1,2] and Xiaohong Joe Zhou[1–4]*

A "featherlike" artifact, termed a *cusp artifact*, is sometimes seen along the phase-encoding direction in sagittal or coronal fast spin echo images. This artifact arises from the spins, at a location distant from the magnet isocenter, that are excited and aliased to the field of view because their precession frequency is similar to those at the isocenter. Such a situation is created due to a combination of excessive gradient nonlinearity and rapid change of the main magnetic field near the edge of the magnet where the artifact-producing spins are located. A novel technique is proposed to reduce this artifact, in which a fast spin echo pulse sequence is modified to slightly tilt the slice selected by the radiofrequency excitation pulse away from the slice selected by the radiofrequency refocusing pulses. At the edge of the field of view, the incomplete overlap between the slices selected by the excitation and refocusing pulses effectively reduces the signals from the artifact-prone region. In contrast, the slices overlap substantially within the field of view so that the signals are largely retained. This slice-tilting technique has been implemented on two commercial MRI scanners operating at 3.0 T and 1.5 T, respectively, and evaluated on phantoms and human spine and extremities using clinical protocols. Both phantom and human results showed that the technique decreased the strength of the cusp artifact by at least 65% and substantially limited the spatial extent of the artifact. This technique, which can be further enhanced by a simple postprocessing step, offers significant advantages over a number of other techniques for reducing the fast spin echo cusp artifact. It can be implemented on virtually any scanner without hardware modification, complicated calibration, sophisticated image reconstruction, or patient-handling alteration. Magn Reson Med 64:220–228, 2010. © **2010 Wiley-Liss, Inc.**

Key words: cusp artifact; annefact; fast spin echo; slice tilt; peripheral signal artifact

The magnetic field gradient in an MRI scanner is linear only within a limited region near the magnet isocenter. Beyond this region, virtually all gradient systems display nonlinear spatial characteristics, particularly at or near the edge of the magnet. This nonideal condition is exacerbated by a rapid change of main magnetic field (B_0) toward the end of the magnet bore. As a result, the overall magnetic field produced by the combination of the gradient field and the B_0 field has a rather complicated spatial dependence. At a region away from the isocenter, the overall magnetic field experienced by spins can be equal to the net magnetic field at or near the magnet isocenter (1) (Fig. 1). The region away from the isocenter, which has been called the "gradient null" (2), is typically outside the imaging volume of interest. If a radiofrequency (RF) coil (or a coil element in a phased array) receives signals from that region, the signal will carry the same (or similar) frequency as the signal near the isocenter, leading to an aliasing artifact in the image. In a fast spin echo (FSE) sequence, the aliasing artifact manifests itself as a series of spots, a band, or a "featherlike" artifact at or near the center of the field of view (FOV) along the phase-encoding direction. The artifact is often observed on sagittal or coronal planes in spine and knee scans (3), interfering with image interpretation. In the literature, this artifact has been called cusp artifact, annefact, foldover artifact, feather artifact, and peripheral signal artifact, along with other names (1–3). Although the cusp artifact does not appear in exactly the same form (i.e., "C"-shaped as shown in Kim et al. (3)) under specific conditions, the mechanism of the artifact formation remains substantially the same. In this work, we refer to this artifact as "cusp artifact", which has been used in several other publications (1–3).

One of the commercial techniques to reduce the artifact relies on adaptive phased-array (APA) coils (4). Individual elements of a phased-array coil can be chosen automatically by an algorithm that determines the proper coil elements based on user-specified FOV while rejecting the signals from coil elements at or near the artifact-prone regions. Although the current literature does not contain a comprehensive evaluation of this approach, it has been observed to be effective under specific conditions (e.g., imaging with limited FOV). To implement the APA technique, substantial modification of the RF receiving electronics and a signal selection algorithm are needed. To avoid the hardware changes, signal-processing techniques based on parallel imaging (e.g., sensitivity encoding (5)) have been used to reduce the FSE cusp artifact (2,6). These techniques estimate the RF field (B_1) sensitivity matrix by utilizing two separate coils, one placed at the magnet isocenter and the other (smaller in size) at or near the artifact-producing region. The nonaliased signal within the FOV can be recovered using a parallel-imaging reconstruction algorithm (5). This approach assumes that the approximate location of the artifact-producing region is known and requires a calibration procedure to estimate the sensitivity matrix for

[1]Center for Magnetic Resonance Research, University of Illinois at Chicago, Chicago, Illinois, USA.
[2]Department of Bioengineering, University of Illinois at Chicago, Chicago, Illinois, USA.
[3]Department of Radiology, University of Illinois at Chicago, Chicago, Illinois, USA.
[4]Department of Neurosurgery, University of Illinois at Chicago, Chicago, Illinois, USA.
*Correspondence to: Xiaohong Joe Zhou, Ph.D., MRI Center, Rm. 1306, Suite 1A, M/C 707, University of Illinois Medical Center, 1801 W. Taylor Street, Chicago, IL 60612. E-mail: xjzhou@uic.edu

Received 25 August 2009; revised 28 January 2010; accepted 3 February 2010.
DOI 10.1002/mrm.22418
Published online in Wiley InterScience (www.interscience.wiley.com).

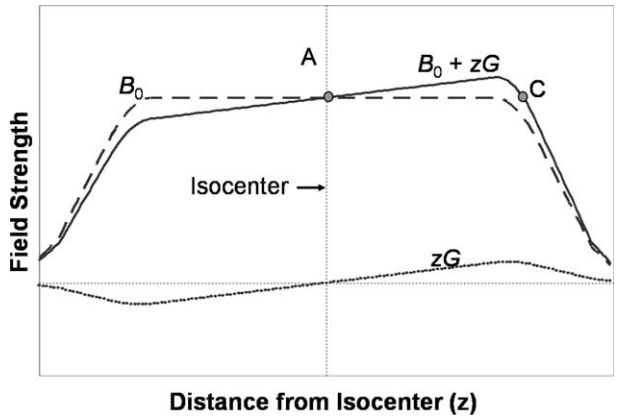

FIG. 1. Profile of $B_{tot} = B_0 + z \times G$ through the bore of the scanner. Due to the nonlinearity of G and rapid change of the main magnetic field (B_0) at or near the edge of the magnet, position C experiences the same net magnetic field as position A at the isocenter, leading to the cusp artifacts.

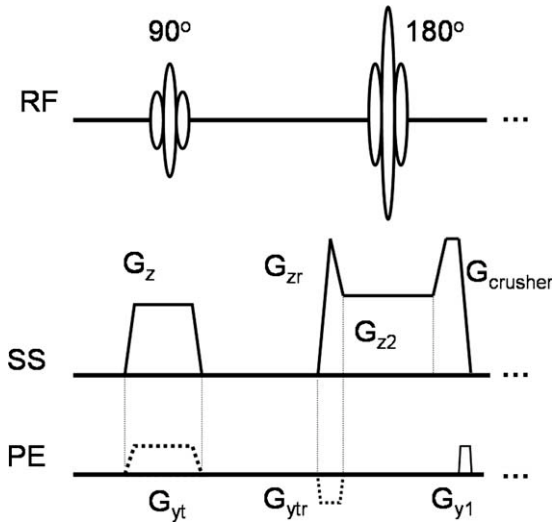

FIG. 2. A segment of the modified FSE pulse sequence, illustrating the slice-tilting gradient G_{yt} and its rewinder G_{ytr} (dotted lines). G_z is the modified slice-selection gradient. G_{zr} is the left crusher gradient combined with the rewinder for G_z.

each RF coil. The assumption and the need for calibration can impose a problem in practical implementation. Another approach entails the use of a metal foil (also known as "metal skirt" or "RF blanket") over the artifact-producing region to dephase the magnetization leading to the artifacts. This technique can be effective when the RF blanket is positioned exactly at the location of the artifact source. However, it can impose a safety concern due to the possibility of increased local heating (7). The safety concern can become prohibitive in a SAR-intensive sequence, such as FSE, particularly at high magnetic fields (e.g., 3.0 T). Other techniques of limited scope have also been proposed (1,2).

In this paper, we demonstrate an alternative technique to reduce the FSE cusp artifact by a simple pulse sequence modification. The proposed technique does not involve any hardware change or coil sensitivity calibration and raises no additional concerns related to the specific absorption rate (SAR) or RF-induced local heating.

MATERIALS AND METHODS

Modifications to the Pulse Sequence

To reduce the FSE cusp artifact, our approach is to modify the FSE pulse sequence so that the slice selected by the RF excitation pulse is slightly tilted with respect to the slice selected by the subsequent RF refocusing pulses. With this modification, peripheral magnetization that would cause the cusp artifact will not experience both RF excitation and refocusing pulses, leading to artifact reduction or even elimination.

This method was implemented in a commercial FSE pulse sequence (GE Healthcare, Waukesha, WI) in which a small "slice-selection" gradient, G_{yt} (Fig. 2), was introduced along a non-slice-selection axis (e.g., the phase-encoding axis, as shown in Fig. 2) concurrently with the nominal slice-selection gradient (along the z-direction by convention) during the RF excitation pulse. With the G_{yt} gradient, the slice selected by the RF excitation pulse was tilted away by a small angle θ_y from the nominal slice selected by the RF refocusing pulses (Fig. 3a,b). Since G_{yt} is concurrent with the nominal slice-selection gradient, the amplitude of the nominal gradient must be

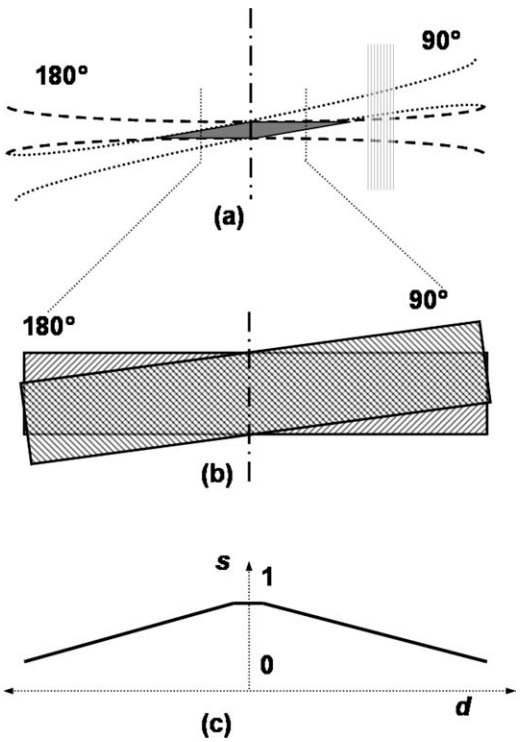

FIG. 3. **a**: Slice profiles for the 90° and 180° RF pulses in FSE, conceptually showing the overlapping region (shaded) and the location of the source of the artifact (vertical lines). The profiles of the slices reflect the nonlinearity of the gradient. **b**: Zoomed profile of slice overlap for the 90° and 180° pulses within the FOV. **c**: Normalized theoretical signal loss s (vertical axis) along the slice tilt direction d (horizontal axis).

adjusted in order to maintain the prescribed slice thickness. The resultant slice-selection gradient G_z and the tilt gradient G_{yt} were calculated by solving the simultaneous equations:

$$\theta_y = \arctan(G_{yt}/G_z) \quad [1]$$

$$G_s^2 = G_{yt}^2 + G_z^2 \quad [2]$$

where G_s is the amplitude of the original slice-selection gradient. For off-centered slices, the transmitter frequency was adjusted accordingly to account for the frequency offset arising from both G_{yt} and G_z.

Similar to the nominal slice-refocusing gradient, an additional slice-refocusing gradient, G_{ytr}, was designed and played together with the left crusher gradient of the first RF refocusing pulse, G_{zr} (Fig. 2). The constraints (e.g., pulse width, slew rate, gradient amplitude) on the design of G_{yt} and G_{ytr} imposed a limit on the maximal value of the user-selectable tilt angle θ_y, beyond which G_{ytr} was unable to completely rephase the spins. This maximum allowable tilt angle was found to be rather large on our system. For example, the maximal tilt angle was more than 70° for a slice thickness of 5 mm with the slew rate set to 90% of the maximum (150 T/m/sec) of our scanner. This tilt angle limit was considerably larger than any tilt angle required for practical implementation (see Results).

Although Fig. 2 illustrates G_{yt} only along the phase-encoding direction, the tilt can also be applied along the readout direction or both the readout and phase-encoding directions. When the slice-tilting gradient is limited to one logical axis, we call it "orthogonal tilt." When the slice-tilting gradient is implemented on both axes, we refer to the tilt as "oblique tilt" to facilitate the following discussions. In the case of oblique tilt, two user-defined tilt angles, θ_x and θ_y, were chosen independently along the two orthogonal axes, respectively. The "slice-selection" gradient on the readout axis, G_{xt}, was designed in a manner analogous to G_{yt}, described by Eq. 1, which involved solving three simultaneous equations (Eqs. 1, 3, and 4).

$$\theta_x = \arctan(G_{xt}/G_z) \quad [3]$$

$$G_s^2 = G_{xt}^2 + G_{yt}^2 + G_z^2 \quad [4]$$

In our sequence design, the slice-rephasing gradient for G_{xt} was combined with the readout prephasing gradient for simplicity and improved time efficiency.

Experiments

The modified FSE pulse sequence was implemented on two GE Signa HDx MRI scanners (GE Healthcare, Waukesha, WI) at 3.0 T and 1.5 T, respectively. Both scanners were equipped with a cardiac resonator module gradient subsystem (maximum gradient strength = 40 mT/m, maximum slew rate = 150 T/m/sec). Using this pulse sequence, a phantom study was performed to determine the optimal tilt angle under several experimental conditions on each of the two scanners. On the 3.0-T scanner, an 18-cm diameter spherical volume (DSV) spherical phantom containing dimethyl silicone, gadolinium, and colorant was placed inside a four-element neurovascular RF coil (USA Instruments, Cleveland, OH). On the 1.5-T scanner, a similar phantom filled with water (18-cm DSV, 3.3685 g/L $NiCl_2.6H_2O$ and 2.4 g/L NaCl) was scanned with an eight-element neurovascular RF coil (Medrad Inc., Indianola, PA). To mimic the source of the FSE cusp artifact, a smaller (11-cm DSV, 3.3685 g/L $NiCl_2.6H_2O$ and 2.4 g/L NaCl) water phantom was placed approximately 22 cm away (i.e., along the positive z-axis) from the isocenter. The position of this phantom was adjusted such that it produced the strongest cusp artifact over a FOV of 24 cm. With this setup (Fig. 4a), the optimal tilt angle was determined as the smallest angle that minimized both the intensity and the extent of the FSE cusp artifact while leaving the signal within the FOV minimally affected. On each scanner, a set of calibration experiments was performed to establish the relationship between the optimal tilt angle and several scan parameters. In the first calibration, the slice thickness was increased from 2 to 10 mm in increments of 2 mm, while keeping all other parameters the same (see below for phantom experiment parameters). At each slice thickness, the optimal tilt angle was determined. In the second calibration, the relationship between the slice thickness and the optimal tilt angle was examined at two additional FOVs: 26 cm and 28 cm. Last, the influence of echo train length (ETL) on the cusp artifact and, consequently, on the optimal tilt angle was investigated by varying the ETL from 4 to 16 in increments of 2.

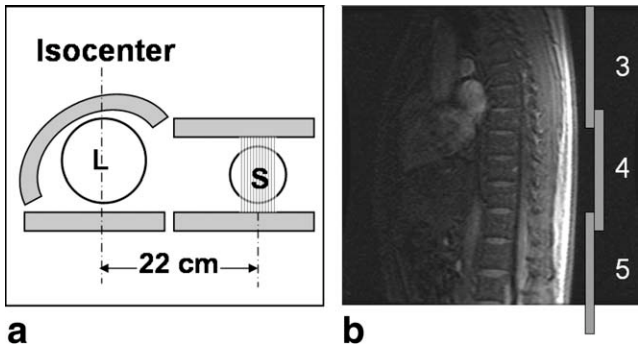

FIG. 4. **a**: Setup of the phantom experiment (experiment 1) using the neurovascular coil (shaded elements), showing the larger (L) and smaller (S) phantoms. The source of the artifact is indicated by the vertical lines. **b**: Setup of the sagittal thoracic spine experiment (experiment 3) showing the approximate locations of the active elements (3–5) of the cervical-thoracic-lumbar coil.

After the optimal tilt angle was determined under different experimental conditions, five experiments were conducted on phantoms or human volunteers to demonstrate and evaluate the performance of the proposed technique. The first experiment was carried out on phantoms (the 18-cm and 11-cm DSV spheres mentioned above) at 3.0 T, with the same setup as described in Fig. 4a. The 18-cm phantom was scanned with a sagittal cervical spine protocol that we used clinically. The key

acquisition parameters were: repetition time (TR) = 2000 ms, echo time (TE) = 10 ms, ETL = 8, bandwidth = 62.5 kHz, acquisition matrix = 256 × 256, number of excitations (NEX) = 2, FOV = 24 cm, slice thickness = 5 mm, and optimal tilt angle $\theta_y = 2.0°$.

The second experiment was to validate the phantom results on human subjects at 3.0 T. The same neurovascular RF coil used in the phantom experiment was employed to obtain images from the left foot of two healthy human subjects (a 26-year-old male and a 31-year-old female) under an approved Institutional Review Board (IRB) protocol. By using the same coil, results from the in vivo human studies can be compared directly with those from the phantom experiments. With the subject in a supine position, a T_1-weighted sagittal foot examination was performed with the following imaging parameters: TR = 600 ms, TE = 20 ms, ETL = 8, bandwidth = 62.5 kHz, acquisition matrix = 256 × 256, NEX = 4, FOV = 26 cm, slice thickness = 5 mm, and optimal tilt angle $\theta_y = 2.0°$. The optimal tilt angle, obtained from the phantom calibration described earlier, was confirmed in one of the human volunteer studies. The artifact-producing region for the in vivo studies was found to be 22.5 ± 1.0 cm away from the isocenter, i.e., the same as in the phantom experiment illustrated in Fig. 4a. The results from the two volunteers were compared to evaluate the performance consistency of the slice-tilting technique.

In the third experiment, we evaluated the performance of the slice-tilting technique in one of our clinical protocols in which the FSE cusp artifact was most problematic. Sagittal images of the thoracic spine were acquired from a 26-year-old male volunteer on the 1.5-T GE Signa scanner using an eight-element cervical-thoracic-lumbar spine coil provided by the equipment manufacturer. The imaging parameters included TR = 3500 ms, TE = 120 ms, ETL = 16, bandwidth = ±15.63 kHz, acquisition matrix = 256 × 256, NEX = 2, FOV = 24 cm, slice thickness = 5 mm, and optimal tilt angle $\theta_y = 2.0°$ with active elements 3 through 5 (Fig. 4b). Since tilting the slice can potentially affect neighboring slices, three contiguous slices without any interslice gap were acquired to evaluate the performance of the slice-tilting technique for multislice imaging.

The fourth experiment was designed to compare the slice-tilting technique with two commercial techniques available on our 3.0-T scanner for FSE cusp artifact reduction. Both commercial techniques were based on a common principle of shifting the source of the cusp artifact. The first technique swapped the position of the artifact source during slice selection by reversing the direction of the slice-selection gradient applied during the 90° RF excitation pulse relative to the slice-selection gradient for the refocusing pulses. The second technique employed a different bandwidth between the RF excitation and refocusing pulses, consequently using a different slice-selection gradient amplitude to dislocate the source of the artifact. In our experimental studies, the bandwidth ratio between the RF excitation and refocusing pulses was varied from 0.5 to 2.0 in steps of 0.5, while keeping the slice thickness constant at 5 mm. Both techniques were evaluated on the left foot of a human volunteer, with the same setup and protocol as described in the second experiment.

The incomplete overlap between the slices selected during the excitation and refocusing pulses will cause the signal intensity at the edge of the FOV to be lower than that at the center. The last experiment was designed to quantify the signal intensity drop at the edge of the FOV as a result of slice tilting. This experiment was conducted on the 3.0-T scanner using the body coil for both RF transmission and reception. Images were acquired from a large (~26-cm DSV) spherical phantom containing dimethyl silicone with the following parameters: TR = 2000 ms, TE = 10 ms, ETL = 16, bandwidth = 62.5 kHz, acquisition matrix = 256 × 256, NEX = 2, FOV = 26 cm. The slice thickness was held constant at 2 mm while the tilt angle was increased from 0° to 3° in steps of 1°. This experiment was repeated with slice thickness of 4, 5, 6, 8, and 10 mm for single-slice and multislice (comprising three slices without interslice gap) acquisitions, respectively.

Optional Postprocessing

In some experiments (e.g., Experiment 1), it was observed that a minor residual artifact (i.e., a thin line in the phase-encoding direction, with a width no more than two to four pixels) remained after the slice-tilting technique substantially reduced both the intensity and the width of the cusp artifact. To further reduce this residual artifact, we have implemented a simple interpolation algorithm that involves the following steps. First, a line containing the residual artifact (i.e., two to four pixels) was zeroed out along the phase-encoding direction of the image. For example, the following operation was executed, assuming that the artifact line was three pixels wide and at the center of the FOV:

$$I(i,j) = 0, \quad 1 \le i \le R, \quad \frac{C}{2} - 1 \le j \le \frac{C}{2} + 1, \qquad [5]$$

where $I(i, j)$ denotes the image intensity of the ith row (i.e., readout direction) and the jth column (i.e., the phase-encoding direction), R is the total number of rows, and C is the total number of columns of the image. Then, along each row, the missing signal intensities were linearly interpolated from the two immediately adjacent pixels. In the example given in Eq. 5, the interpolation was performed in the following manner:

$$\begin{bmatrix} I(i,\frac{C}{2}-1) \\ I(i,\frac{C}{2}) \\ I(i,\frac{C}{2}+1) \end{bmatrix} = \frac{1}{4}\begin{bmatrix} 1 & 3 \\ 2 & 2 \\ 3 & 1 \end{bmatrix}\begin{bmatrix} I(i,\frac{C}{2}+2) \\ I(i,\frac{C}{2}-2) \end{bmatrix}, \quad 1 \le i \le R \qquad [6]$$

The use of this interpolation algorithm was optional, depending on the presence and severity of the residual artifact.

Artifact Evaluation

The FSE cusp artifact was first visually compared before and after applying the slice-tilting technique, followed by a quantitative analysis of the artifact strength. In the quantitative analysis, three regions of interest (ROIs),

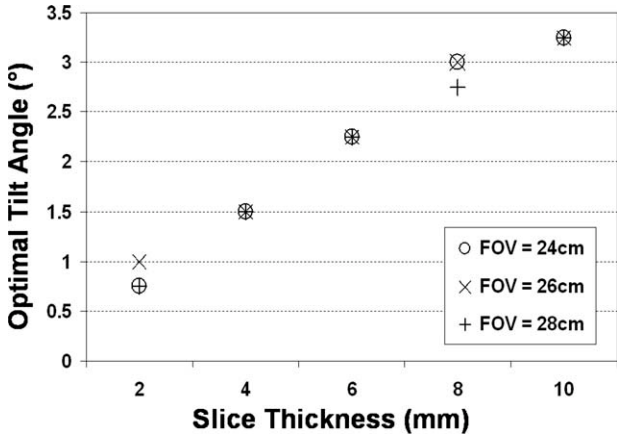

FIG. 5. Optimal tilt angle θ_y as a function of slice thickness for three different FOV.

each comprising ~100 pixels, were selected from (i) a homogeneous region (10 × 10 pixels) of the object with the highest signal intensity (e.g., on the calcaneus of the foot of the volunteer, or on the subcutaneous fat of the thoracic images from the volunteer), (ii) the background (10 × 10 pixels) free of artifacts, and (iii) the area with the strongest artifact strength (10 × 10 or 20 × 5 pixels, depending upon the appearance of the artifact). The strength of the artifact (s_a) was quantified using the following equation:

$$s_a = \frac{\mu_a - \mu_n}{\mu_o - \mu_n}, \quad [7]$$

where μ_o, μ_a, and μ_n were the mean signal intensity of the ROIs over the object, the artifact, and the background, respectively.

Evaluation of Signal Uniformity

Signal uniformity was evaluated in the direction of the slice tilt (i.e., the phase-encoding direction) for all images acquired in the fifth experiment. Two ROIs, each comprising ~100 pixels, were selected from (i) the highest signal region (10 × 10 pixels) at or near the center of the spherical phantom, and (ii) the lowest signal region (10 × 10 pixels) within 2.5 cm of the edge of the FOV on the phantom in the direction of the tilt. The signal uniformity, U, was calculated using the following equation:

$$U = 1 - \frac{\mu_c - \mu_e}{\mu_c + \mu_e}, \quad [8]$$

where μ_c and μ_e were the mean signal intensity of the ROIs taken at the center and the edge, respectively.

RESULTS

Figure 5 shows the optimal tilt angle obtained from the phantoms on the 3.0-T scanner as a function of the slice thickness for FOVs of 24, 26, and 28 cm, respectively. In all cases, the relationship between the slice thickness and the optimal tilt was found to be approximately linear (e.g., $r = 0.9883$ for FOV = 24 cm). The same relationship was confirmed for human volunteers, suggesting that the optimal tilt angles obtained on a phantom scan were usable for other scans with the same or similar slice thickness. The dependence of the optimal tilt angle on the FOV was very weak (Fig. 5), and no dependence on ETL was observed (data not shown). Similar results were also obtained from the other scanner (data not shown).

A representative result from the first (phantom) experiment is shown in Fig. 6, where an unconventional window/level setting was used to highlight the artifact. The cusp artifact is enclosed in a dashed box on the images. (Note that the typical FSE ghosting artifacts can also be seen on the lower left side of the images. These artifacts are unrelated to the FSE cusp artifact described in this paper.) By applying a tilt of 2° for a slice thickness of 5 mm over a FOV of 24 cm, the strength of the cusp artifact was reduced from 16.3% (Fig. 6a) to 5.3% (Fig. 6b). As a result of this substantial reduction, the featherlike structure virtually disappeared and the width of the remaining artifact was noticeably narrowed. The residual artifact strength was further reduced to ~1.8% (Fig. 6c) using the optional postprocessing step detailed in the Materials and Methods section.

The results from the second experiment on human foot images at 3.0 T are shown in Fig. 7, where an unconventional window/level setting was used to

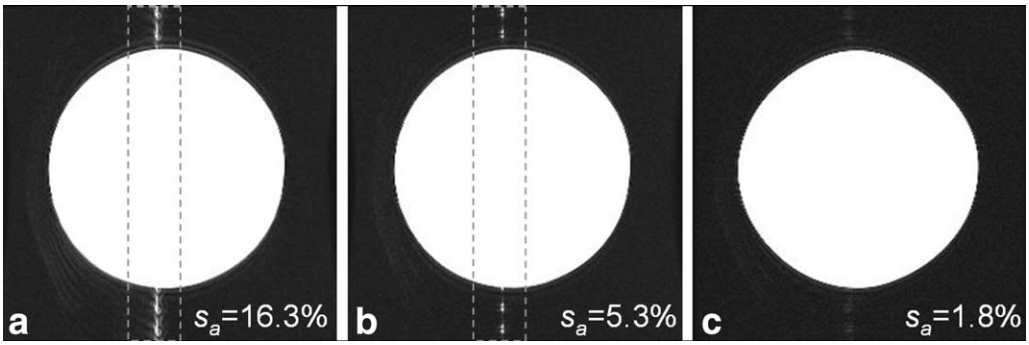

FIG. 6. FSE images of an 18-cm (DSV) phantom (**a**) without slice-tilting, (**b**) with tilt angle = 2°, and (**c**) with tilt angle = 2° and postprocessing described by Eqs. 5 and 6. All images were obtained at 3.0 T using a four-element neurovascular coil. An unconventional window/level setting was used to highlight the cusp artifact, which is within the dashed box in (**a**) and (**b**). TR/TE = 2000/10 ms, FOV = 24 cm.

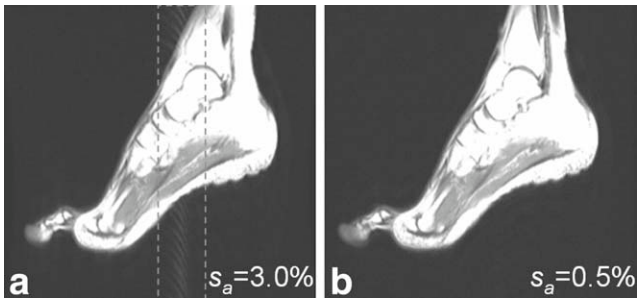

FIG. 7. FSE images of human foot at 3.0 T (**a**) without slice tilting and (**b**) with slice tilting ($\theta_y = 2°$). An unconventional window/level setting was used to highlight the artifacts, which are shown within the dashed box. TR/TE = 600/20 ms, FOV = 26 cm.

emphasize the artifacts. On one of the volunteers, the artifact strength was reduced from 3.0% (Fig. 7a) before to 0.5% (Fig. 7b) after applying a tilting angle of 2.0°. The artifacts in the resultant image were essentially invisible, even with a window and level setting to highlight the low signal intensities. Results from the second human volunteer showed a similar performance, with the artifact strength decreasing from 5.1% to 0.9% before and after the tilt (images not shown), demonstrating good intersubject consistency of the slice-tilting technique.

An even better performance was obtained in the human thoracic spine study (i.e., the third experiment) at 1.5 T. Figure 8 shows two of the three contiguous sagittal slices before (Fig. 8a,b) and after (Fig. 8c,d) applying the slice-tilting technique. Before tilting, the characteristic featherlike artifacts were evident along the superior-inferior direction (i.e., the phase-encoding direction), with artifact strength as high as 14.0% (Fig. 8b) to 28.7% (Fig. 8a). After tilting, the artifact strength was reduced to 2 ~ 3% (Fig. 8c,d), which was virtually invisible despite a window and level setting to emphasize the artifact. It is worth noting that no significant image shading was observed across the FOV after applying the slice-tilting technique. Additionally, the effect of crosstalk in the multislice acquisition was insignificant even with a tilt angle of 2°, without any interslice gap.

Figure 9 summarizes the results of the fourth experiment, which compares the slice-tilting technique with the two commercially available techniques. Figure 9a displays the original image without any compensatory techniques. Figure 9b and c shows the result of reversing the slice-selection gradient and varying the bandwidth of the RF excitation pulse to twice the original bandwidth (a bandwidth ratio of 2 was experimentally observed to give the best artifact reduction for this technique), respectively. The result of the slice-tilting technique (tilt angle = 2°) is given in Fig. 9d. Visual inspection of these images clearly showed that the slice-tilting technique outperformed the two commercial techniques.

The results of the signal uniformity evaluation on the phantom are summarized in Fig. 10. Figure 10a shows the values of percentage signal uniformity as a function of slice thickness and tilt angle for single-slice imaging. For example, for a slice thickness of 5 mm and a tilt angle of 2°, the intensity uniformity was found to be 71%. The uniformity values for single-slice imaging are comparable to those in multislice imaging (Fig. 10b), suggesting that the slice-tilting technique has minimal adverse effect in multislice acquisitions. Figure 10c compares the profiles of signal intensity for tilt angles from 0° to 3° for a 5 mm slice (single-slice acquisition) along

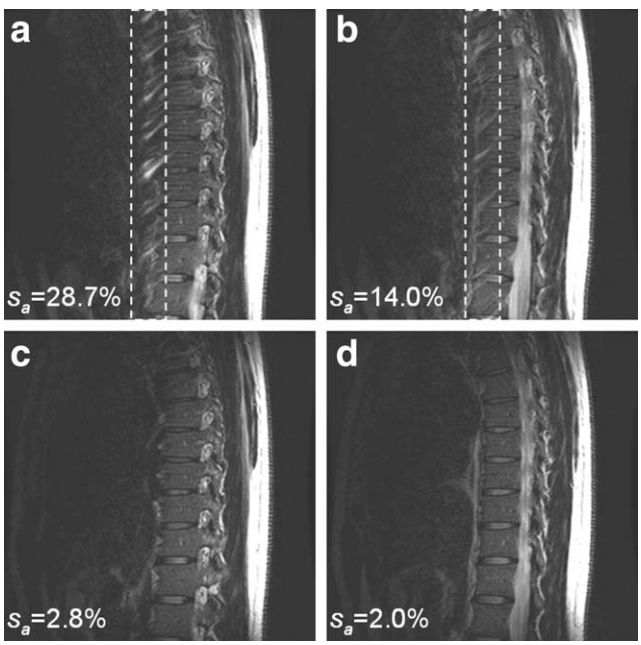

FIG. 8. Two adjacent sagittal images of the thoracic spine at 1.5 T (slice thickness = 5 mm; slice gap = 0 mm) (**a,b**) without slice-tilting and (**c,d**) with slice tilting ($\theta_y = 2°$). TR/TE = 3500/120 ms, FOV = 24 cm.

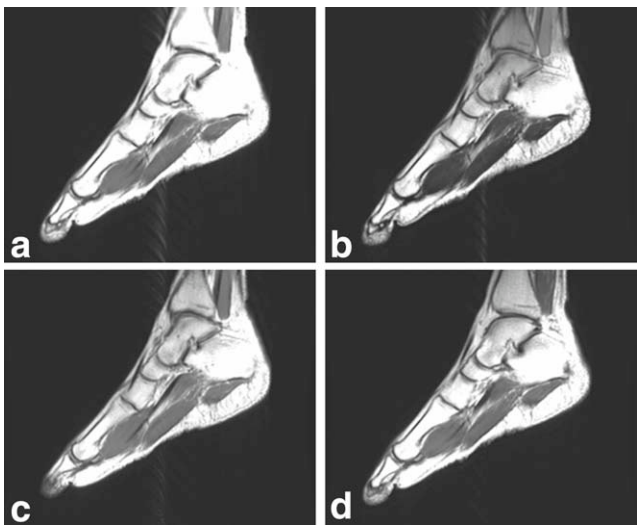

FIG. 9. Sagittal foot FSE images from a human volunteer, comparing the slice-tilting technique with two commercially available techniques. **a**: Original image. **b**: Image obtained by reversing the direction of the slice-selection gradient during the RF excitation pulse. **c**: Image obtained by increasing the bandwidth of the RF excitation pulse to twice of that of the RF refocusing pulse. **d**: Image with slice tilting ($\theta_y = 2°$). An unconventional window/level setting was used to highlight the artifacts. TR/TE = 600/20 ms and FOV = 26 cm.

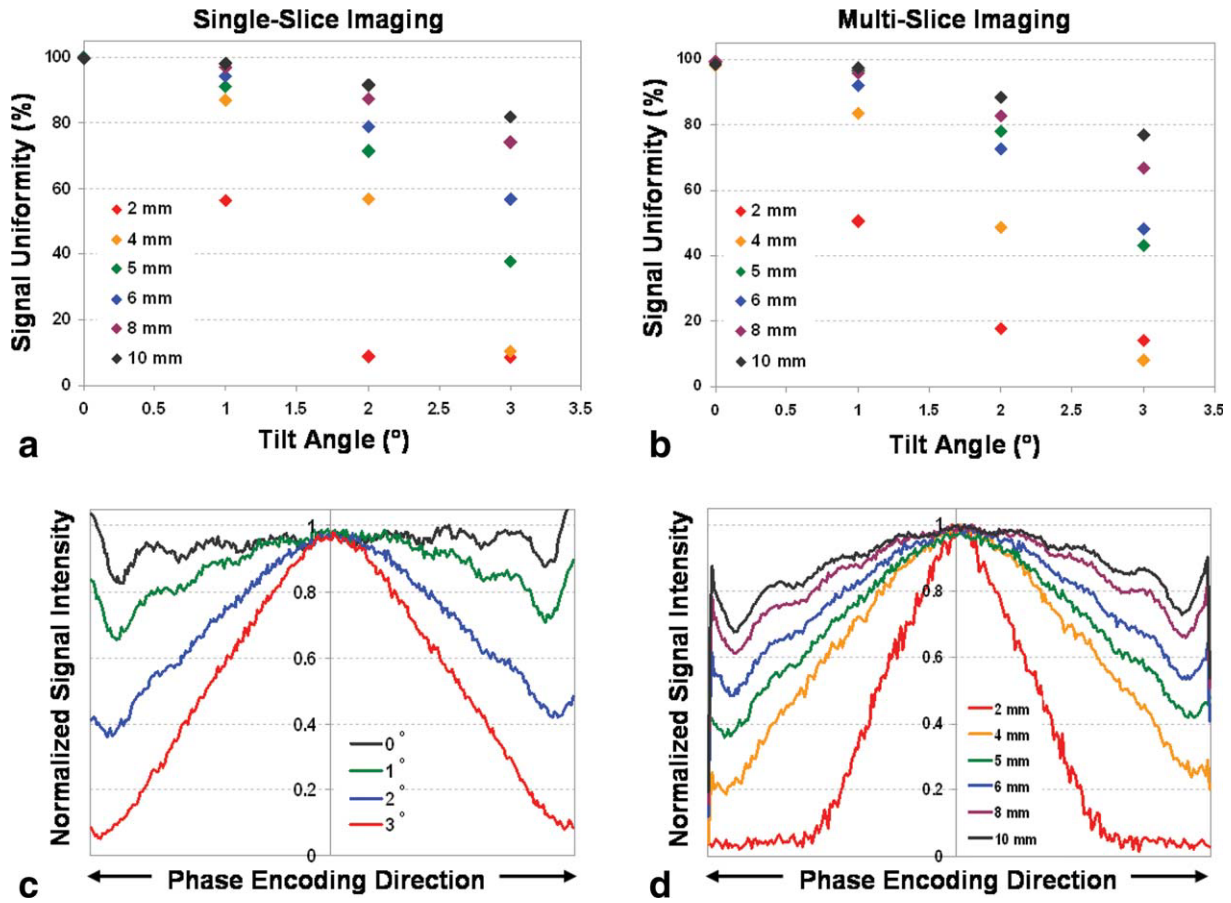

FIG. 10. Signal nonuniformity in the direction of the slice tilt (i.e., the phase-encoding direction). **a**: Signal uniformity as a function of slice thickness in single-slice imaging (θ_y = 0–3°). **b**: Signal uniformity as a function of slice thickness in multislice imaging (central slice, slice gap = 0 mm). **c**: Normalized signal intensity profiles in the phase-encoding direction as a function of tilt angle (slice thickness = 5 mm; single-slice acquisition). **d**: Normalized profiles of signal intensity in the phase-encoding direction as a function of slice thickness (tilt angle = 2°; single-slice acquisition). TR/TE = 2000/10 ms and FOV = 24 cm.

the central column in the phase-encoding direction. For a typical tilt angle (2°) used in all experiments, the worst signal drop was about ~40% as compared to the signal at the center. The dependence of the signal loss on slice thickness is shown in Fig. 10d, where the tilt angle was held constant at 2° in a single-slice acquisition. The signal loss became progressively worse as the slice thickness decreased, especially below 4 mm. However, as the slice becomes thinner, the required tilt angle also decreases (Fig. 5), which substantially compensates for the signal loss illustrated in Fig. 10a–c.

DISCUSSION

In this study, we have observed that a small slice-tilting gradient along a non-slice-selection axis during RF excitation can significantly reduce the intensity (by ≥65%) and the extent of the FSE cusp artifact. The optimal tilt angle can be determined by using a simple calibration procedure on a phantom and applied to a broad range of protocols encountered in clinical imaging. The dependence of the optimal tilt angle on slice thickness, FOV, and ETL has been studied, which revealed a linear relationship with respect to slice thickness and no significant dependence on FOV or ETL. This technique was validated on scanners operating at two different field strengths, multiple RF coils, a number of clinical protocols, and both phantoms and human volunteers. Consistent and reproducible artifact reduction was observed in all cases.

Compared to existing methods for FSE cusp artifact reduction, the slice-tilting technique offers a number of advantages. First, unlike the APA method, the slice-tilting technique requires no change in the system hardware. As such, it is easy to implement and applicable to virtually all scanners where the FSE cusp artifact is problematic. Second, the slice-tilting technique imposes no changes in image reconstruction algorithms. This is in sharp contract to the parallel imaging approaches in which the coil sensitivity profiles must be incorporated into image reconstruction (2,6). Third, the calibration procedure in the slice-tilting technique is simple and straightforward. It does not require an additional RF coil to acquire signals from the artifact-prone region and one calibration can be used for a number of clinical protocols. Since the optimal tilt angle spans a very small range under most circumstances, the calibration procedure may even be eliminated by using a generic tilt angle

in the range of 1–3°, as further discussed below. Fourth, compared with methods such as the application of an RF blanket, the slice-tilting technique imposes neither additional safety concerns nor changes in patient handling. Last, the slice-tilting technique has exhibited better performance in FSE cusp artifact reduction when compared with two other commercially available techniques in which the slice-selection gradient polarity or the amplitude is manipulated in pulse sequence design (Fig. 9). In addition, the slice-tilting technique can also avoid the problem with chemical shift and other off-resonance effects encountered by the commercial techniques because of the change in either gradient polarity or amplitude.

Although the primary focus of this study is not to characterize the appearance of the FSE cusp artifact, we have observed that the strength of the artifact was inversely proportional to the slice thickness. For example, the artifact strength increased from 11.2% to 21.9% when the slice thickness decreased from 8 to 4 mm. This dependence was most likely related to the amplitude of the slice-selection gradient. A thinner slice requires a stronger gradient, which can move the artifact-prone region closer to the sensitive region of the RF receiving coil, leading to a stronger artifact. This explanation is in agreement with the fact that the bandwidth of the RF pulse (and thus the slice-selection gradient amplitude) can alter the appearance of the FSE cusp artifact, as exploited in one of the commercial techniques evaluated in our study (Fig. 9c). Interestingly, in our experimental study on human subjects, we observed no monotonic relationship between the artifact intensity and the RF excitation bandwidth. This is possibly because the continuous distribution of spins in human subjects can support a broad range of artifact-prone regions. This is different from the situation in our calibration scan where the artifact-prone region was limited to a specific location. This observation suggests that although the slice-tilting technique can be effective to avoid artifact arising from a specific location, artifact reduction may not be complete when the artifact source spans a broader region. This may explain the residual artifact after slice-tilting that we have seen in some experimental studies (e.g., Fig. 6b).

Another possible source for the residual artifact may arise from the location where the spatial derivative of the overall magnetic field $B_{tot} = B_0 + z \times G$ is zero. At this location, the slice orientation may not be effectively tilted by a tilting gradient. Since this location theoretically corresponds to only a point, the resulting residual artifact is expected to have a very narrow width, essentially turning the "feather" artifact into a thin dotted line (two to four pixels wide), as we observed in Fig. 6b. We have demonstrated that the simple interpolation technique can further reduce this residual artifact, as shown in Fig. 6c. Since the column to be regenerated was very thin (typically two to four pixels), linear interpolation did not significantly blur the image, especially when the signal change was gradual. This interpolation algorithm was not necessary in many situations (e.g., Figs. 7 and 8) and should be used on an as-needed basis either prospectively or retrospectively.

The calibration results in Fig. 5 indicate that even though the artifact intensity was higher with a thinner slice, a smaller slice tilt was needed to create a sufficient mismatch between the slices selected by the excitation pulse and the refocusing pulses at the artifact-producing region. This geometric consideration is most likely the reason behind the linear relationship between the optimal tilt angle and the slice thickness. The two outlying points seen in Fig. 5 are within the measurement accuracy (~0.25°), as the minimum step size in θ_y was 0.25° in the calibration. Even with the dependence on the slice thickness, the optimal tilt angle spanned only a very narrow range (1.3 ~ 2.3°) for a slice thickness between 3 and 6mm. From a practical perspective, a nominal tilt angle of ~2° can be used as a default when the calibration data are not available or intentionally omitted. This can greatly simplify practical implementation of the technique.

The proposed slice-tilting technique does have several limitations. A primary issue is the reduction in the signal away from the slice center (Figs. 3c, 10) because of reduced overlap between slices selected by the excitation and refocusing pulses (Fig. 3b). For a FOV of 24 cm, with a 5 mm slice thickness and a tilt angle of 2°, the theoretically calculated signal intensity at the edge of the FOV was only a small fraction (e.g., ~20%) of the signal without the tilt. This calculation assumed (i) an ideal gradient linearity, (ii) a uniform RF coil sensitivity profile across the FOV, and (iii) a homogeneous signal intensity distribution within the slice. However, increased gradient nonlinearity (i.e., a weaker gradient) at the edge and higher B_1 field sensitivity can make the intensity shading effect much less obvious (Figs. 10c,d). The compensatory effect from the B_1 field is particularly important when a phased-array coil is employed, analogous to using multielement RF coils to offset the "center-brightening" artifacts in high-field (e.g., 3.0 T) imaging. Because of these compensatory mechanisms, the experimentally observed signal intensity near the edge of the FOV was at least 60% of the signal intensity at the center for the FOVs and tilt angles used in this study. Further, the signal uniformity was maintained at 60–80% under most practically encountered conditions (Fig. 10a,b). If necessary, the signal shading associated with slice tilting can be corrected for by using techniques similar to those used for surface coil intensity correction (8,9). Since the intensity loss can be estimated by theoretical analysis (Fig. 3c), as well as experimental studies (Fig. 10), algorithms for shading correction are expected to be very feasible.

Another concern on the proposed artifact reduction technique is its robustness for multislice imaging. With a tilted slice, interslice interference becomes progressively worse toward the edge of the FOV. However, with a conventional odd/even slice reordering scheme, we have observed in Fig. 8 that the slice-tilting technique works remarkably well even without any slice gap. Figure 10b further shows that the signal uniformity due to slice tilting was approximately the same irrespective of single-slice or multislice acquisitions, indicating that slice crosstalk was insignificant in the slice-tilting technique. In the rare event that this problem becomes significant, it can be mitigated by slice reordering. For example, the slice

order may follow a sequence such as (1,4,7,10) → (2,5,8,11) → (3,6,9,12), instead of the typical odd/even slice ordering. If a contiguous slice ordering must be used, the interslice spacing can be adjusted to address this problem. Theoretically, the minimum slice spacing required for contiguous slice ordering can be calculated from:

$$sp = \tan\theta \times \frac{FOV}{2} + (\sec\theta - 1)\frac{th}{2}, \quad [9]$$

where *sp* is the slice gap, *th* is slice thickness, and θ is the tilt angle. For example, when FOV = 24 cm, *th* = 5 mm, and θ = 2°, *sp* was estimated to be ~4 mm. It is worth noting that T_1 relaxation can also help recover the perturbed signals caused by tilting of the neighboring slices. Thus, the theoretical result given by Eq. 9 only represents the worse-case scenario and most likely will not be encountered unless contiguous slice ordering is used on spins with long T_1s.

The third limitation of the proposed technique arises from its assumption that the artifact-producing region resides in a defined location outside the FOV. While this assumption is valid in the majority of cases, physiologic motion (such as respiration) can dynamically alter the artifact-producing region, which causes the artifact to have a smeared appearance and increases the challenge associated with its reduction. This problem may be addressed by incorporating one of the motion-correction or -compensation techniques into slice-tilting, which is an area of further investigation.

Although all results presented in this paper were obtained using an orthogonal tilt approach (see the Materials and Methods section), the oblique tilt approach was also implemented by including two tilting angles, as described by Eqs. 1 and 3. Our experimental studies with oblique tilt indicated that the improvement over orthogonal tilt was not substantial. For example, in an experiment conducted on a phantom, the strength of the artifact decreased from 1.9% without applying any tilt angle to 0.7% with $\theta_x = 0°$ and $\theta_y = 2°$, and 0.65% with $\theta_x = \theta_y = 2°$. Additionally, the oblique tilt approach also exhibits a more complicated signal shading pattern. Although no significant benefit has been observed in the oblique tilt approach thus far, it does provide an additional degree of freedom to address the FSE cusp artifact and may prove useful in situations that have not been encountered in this study.

Our focus in this study is to reduce the FSE cusp artifact using a slice-tilting gradient. The same concept can be expanded to address problems in other areas. One potential application is to restrict the FOV in a manner similar to Symms et al. (10). For this application, the prescribed slice can be selected by a combination of an RF excitation pulse and an oblique slice-selection gradient concurrent with an RF refocusing pulse to restrict the signal-producing region. This is analogous to inner-volume imaging techniques that have already been demonstrated in localized spectroscopy (11) and imaging (12). Another application is to extend the concept to PROPELLER imaging (13) in order to reduce aliasing artifacts when the phase-encoding direction of a PROPELLER blade is along the long dimension of an imaged object (14,15). For these potential applications, it is possible that the oblique tilt approach may play a larger role.

CONCLUSION

We have demonstrated that the introduction of a small tilt in slice selection during the RF excitation pulse can considerably decrease the FSE cusp artifact. This approach involves only a simple modification to the pulse sequence, together with an easy calibration procedure without any change to the hardware, patient handling, or image reconstruction algorithms. The image is produced in final or near-final form at the end of the scan and can be further improved with a straightforward postprocessing step. This simple yet effective approach can be applied to virtually all MRI scanners in which the FSE cusp artifact is problematic.

ACKNOWLEDGMENTS

This work was supported partially by a grant from CCTS of the University of Illinois Medical Center at Chicago. The authors thank Girish Srinivasan, Yi Sui, Qing Gao, Hagai Ganin, and Michael Flannery for their technical assistance and Dr. Keith R. Thulborn for helpful discussions.

REFERENCES

1. Steckner MC, Dannels W. The FSE "cusp" artifact: interactions between RF rolloff, gradient rollover, and B0 homogeneity. In: ISMRM Abstracts, Nice, France, 1995. p 756.
2. King KF, Hinks RS. General Electric Company, assignee. Method and system of MR imaging with reduced FSE cusp artifacts. USA patent 7250762. 2007.
3. Kim JK, White LM, Hinks RS, King KF. The FSE cusp artifact: a phase wrap-in artifact seen on routine clinical MR images of the knee. In: ISMRM Abstracts, Philadelphia, PA, 1999. p 1033.
4. Frederick P, Johnson J; General Electric Company, assignee. Method for reducing artifacts in MR image acquired with phased array surface coil. USA patent 6134465. 2000.
5. Pruessmann KP, Weiger M, Scheidegger MB, Boesiger P. SENSE: sensitivity encoding for fast MRI. Magn Reson Med 1999;42:952–962.
6. Larkman DJ, Herlihy AH, Coutts GA, Hajnal JV. Elimination of magnetic field foldover artifacts in MR images. J Magn Reson Imaging 2000;12:795–797.
7. Schaefer DJ. Safety aspects of radiofrequency power deposition in magnetic resonance. Magn Reson Imaging Clin N Am 1998;6:775–789.
8. Axel L, Costantini J, Listerud J. Intensity correction in surface-coil MR imaging. AJR Am J Roentgenol 1987;148:418–420.
9. Vovk U, Pernus F, Likar B. A review of methods for correction of intensity inhomogeneity in MRI. IEEE Trans Med Imaging 2007;26:405–421.
10. Symms MR, Wheeler-Kingshott C, Parker GJM, Barker GJ. Zonally-magnified oblique multislice (ZOOM) EPI. In: ISMRM Abstracts, Denver, CO, 2000. p 160.
11. Bottomley PA. Spatial localization in NMR spectroscopy in vivo. Ann N Y Acad Sci 1987;508:333–348.
12. Feinberg DA, Hoenninger JC, Crooks LE, Kaufman L, Watts JC, Arakawa M. Inner volume MR imaging: technical concepts and their application. Radiology 1985;156:743–747.
13. Pipe JG. Motion correction with PROPELLER MRI: application to head motion and free-breathing cardiac imaging. Magn Reson Med 1999;42:963–969.
14. Rangwala NA, Srinivasan G, Zhou XJ. Reduction of aliasing artifacts in diffusion-weighted PROPELLER imaging. In: ISMRM Abstracts, Honolulu, HI, 2009. p 2683.
15. Deng J, Larson AC. Multishot targeted PROPELLER magnetic resonance imaging: description of the technique and initial applications. Invest Radiol 2009;44:454–462.